

Alma Mater Studiorum Università di Bologna  
Archivio istituzionale della ricerca

Influence of Nozzle Radiation on Solid Rocket Motors Tail-Off Thrust

This is the final peer-reviewed author's accepted manuscript (postprint) of the following publication:

*Published Version:*

Fabrizio Ponti, Stefano Mini, Luca Fadigati, Adriano Annovazzi, Enrico Corti (2021). Influence of Nozzle Radiation on Solid Rocket Motors Tail-Off Thrust. INTERNATIONAL JOURNAL OF ENERGETIC MATERIALS AND CHEMICAL PROPULSION, 20(3), 45-64 [10.1615/IntJEnergeticMaterialsChemProp.2021038491].

*Availability:*

This version is available at: <https://hdl.handle.net/11585/826562> since: 2024-05-10

*Published:*

DOI: <http://doi.org/10.1615/IntJEnergeticMaterialsChemProp.2021038491>

*Terms of use:*

Some rights reserved. The terms and conditions for the reuse of this version of the manuscript are specified in the publishing policy. For all terms of use and more information see the publisher's website.

This item was downloaded from IRIS Università di Bologna (<https://cris.unibo.it/>).  
When citing, please refer to the published version.

(Article begins on next page)

# Influence of Nozzle Radiation on Solid Rocket Motors Tail-off Thrust

## **Fabrizio Ponti**

Full Professor, Department DIN, via Fontanelle 40; fabrizio.ponti@unibo.it

## **Stefano Mini**

Ph.D. Candidate, Department DIN, via Fontanelle 40; stefano.mini3@unibo.it

## **Luca Fadigati**

Ph.D. Candidate, Department DIN, via Fontanelle 40; luca.fadigati2@unibo.it

## **Adriano Annovazzi**

Senior Engineer, AVIO Space Propulsion Design Department, Rome;  
adriano.annovazzi@avio.com

## **Enrico Corti**

Associate Professor, Department DIN, via Fontanelle 40; enrico.corti2@unibo.it

## **Abstract**

The aims of this work are focused on the evaluation of the solid rocket motor residual thrust and on the impact of thermal protection properties on such thrust. Indeed, tail-off thrust of solid rocket motors upper stages can last tens of seconds after motor burn-out, affecting the performance of the rocket on sequencing of stage separation. Hence, the knowledge of the tail-off thrust profile is fundamental to properly design wait times and separation systems total impulse of a multi-stage launcher. Therefore, although it has been shown in the past that pyrolysis gases responsible for the residual thrust are mostly produced by alumina molten slag deposited next to the nozzle nose within the combustion chamber, this study is aimed at suggesting that the portion of the nozzle within the combustion chamber can act as the main radiative heat source leading to thermal protection material ablation, and then to residual thrust production. An analysis of an actual solid rocket motor has been performed in the direction of proving the effectiveness of the overall procedure. Then a sensitivity analysis with respect to the quantities identifying the thermal protection properties has been computed in order to evaluate the impact of such variations on the residual thrust profile.

## **Key Words**

Solid rocket motor, thermal protection, charring ablator, residual thrust, ablation.

## **Nomenclature**

### **Latin**

$A$	=	cross-section thermal protection material area, $m^2$
$A_{TP}$	=	thermal protection material area, $m^2$
$B$	=	Arrhenius constant, $1/s$
$c_p$	=	specific heat, $J/kg \cdot K$
$E_a$	=	Arrhenius activation energy per unit mole, $J/mol$

$H$	=	enthalpy per unit mass, $J/kg$
$\bar{H}$	=	weighted average enthalpy per unit mass, $J/kg$
$K_1$	=	first char erosion constant, $m^2 \cdot K/W$
$K_2$	=	second char erosion constant, -
$h_c$	=	heat transfer convective coefficient, $W/m^2 \cdot K$
$K_{Nu}$	=	Nusselt constant
$k$	=	thermal conductivity, $W/m \cdot K$
$L$	=	thermal protections thickness, $m$
$M$	=	mass flow rate per unit surface, $kg/s \cdot m^2$
$\dot{m}$	=	mass flow rate, $kg/s$
$Nu$	=	combustion chamber Nusselt number
$Pr$	=	combustion chamber Prandtl number
$\dot{Q}_{abs}$	=	thermal power absorbed by ablative material from combustion chamber
		per unit surface, $W/m^2$
$\dot{Q}_{cond}$	=	thermal conduction power per unit surface, $W/m^2$
$\dot{Q}_{conv}$	=	thermal convective power per unit surface, $W/m^2$
$\dot{Q}_{in}$	=	chemical power per unit surface from in-depth material, $W/m^2$
$\dot{Q}_{noz}$	=	nozzle radiative power per unit surface, $W/m^2$
$\dot{Q}_{out}$	=	chemical power per unit surface exiting from the material due to blowing
		effect, $W/m^2$
$\dot{Q}_{radin}$	=	radiative power per unit surface entering the material, $W/m^2$
$\dot{Q}_{radout}$	=	radiative power per unit surface exiting the material, $W/m^2$
$R$	=	universal gas constant, $J/mol \cdot K$
$r_b$	=	propellant burning rate, $m/s$
$\dot{s}$	=	char recession rate, $m/s$
$t$	=	time, $s$
$t_0$	=	reference time instant, $s$
$T$	=	temperature, $K$
$T_I$	=	initial thermal protection temperature, $K$
$T_0$	=	formation temperature, $K$
$V_F$	=	view factor between nozzle and rocket case
$x$	=	spatial coordinate, $m$

### Greek

$\alpha$	=	weighted average between virgin material and char specific heats,
		$J/kg \cdot K$
$\alpha_s$	=	ablative material absorptivity, -
$\beta$	=	weighted average between virgin material and char specific heats
		difference, $J/kg \cdot K$
$\varepsilon$	=	emissivity, -
$\eta$	=	weighted average between virgin material and char thermal
		conductivities, $W/m \cdot K$
$\xi$	=	weighted average between virgin material and char conductivities
		difference, $W/m \cdot K$
$\rho$	=	density, $kg/m^3$
$\sigma$	=	Stefan-Boltzmann constant, $W/m^2 \cdot K^4$
$\varphi$	=	blowing parameter, -
$X$	=	virgin material mass fraction, -

$\psi$	=	Arrhenius exponent, -
$\tau$	=	gas shielding factor linked to optical length, -

### Subscripts

$c$	=	char material
$g$	=	pyrolysis gas
$gas$	=	combustion chamber hot gases
$p$	=	propellant
$v$	=	virgin material

### Superscripts

'	=	integration variable
$o$	=	formation enthalpy

### Acronyms

BVP	=	Boundary Value Problem
CEA	=	Chemical Equilibrium and Applications
CMA	=	Charring Material thermal response and Ablation program
FIAT	=	Fully Implicit Ablation and Thermal analysis program
NASA	=	National Aeronautics and Space Administration
ROBOOST	=	ROcket BOOst Simulation Tool
SRM	=	Solid Rocket Motor
Z23	=	ZEFIRO 23
ZEFIRO 9	=	ZERO First stage ROcket 9
ZEFIRO 23	=	ZERO First stage ROcket 23

## 1. Introduction

In the design of a solid rocket motor (SRM), the performance prediction in terms of thrust-time profile assumes a fundamental role in the design process [1]. From a general perspective, SRMs rely on a basic layout, without any complex system as turbomachinery devices common to liquid propellant engines. However, the absence of any component able to switch off grain combustion, implies no possibility of thrust control or rocket shut off after propellant ignition. Therefore, thrust estimation acquires an essential role as a trade-off between the capability of predicting rocket performance as close as possible to the actual one and the need of bound the cost impact associated with experimental firing tests.

The thrust-time profile consists of three main phases [2]: ignition transient, quasi-steady state phase, and tail-off. Although the first and the last ones, respectively regarding the initial and final thrust production period, are very bounded in time, they are strongly time dependent. On the other side, quasi-steady state behavior represents the 90÷95% of the grain combustion duration and it is propellant burning driven. More in detail, tail-off thrust is of particular interest because of the potential deviations from the nominal performance. Some unsteady phenomena, like residual thrust generation [3], can occur at that phase. In fact, as disclosed by experimental observations [3], tail-off duration can last tens of seconds after the complete depletion of the propellant, and therefore this occurrence cannot be neglected in motor design. In fact, tail-off thrust prediction is fundamental for the proper sequencing of stage separation meaning an effective handling of interstage wait times and interstage separation systems total impulse. In past literature [3-6] it is reported that the primary cause of the above-mentioned event relies on the pyrolysis gas production through case-insulating thermal protection ablation. In addition to that, it is proven that material ablation can be induced by the radiative power linked to molten slag mass [7-10]. The molten slag is composed of aluminum and alumina residue from the

combustion of aluminized solid propellant, and the magnitude of slag accumulation is driven by the radial and/or axial rocket acceleration. The slag occurrence in the combustion chamber influences motor performance, leading to controllability issues with respect to the rocket attitude or generating an amount of radiative power sufficient to trigger the case-insulating thermal protection material ablation. However, in the experimental firing test regarding the solid rocket motor considered in this work, no slag presence has been identified. Such observation implies that another source can lead to the insulating material ablation. In the present work, such source is identified at the nozzle region within the combustion chamber (Figure 1d). In fact, that surface, warmed up by high-temperature combustion gases, acts as heat source determining thermal protection material ablation even if grain combustion is completely concluded.

Case-insulating material usually relies on *charring* ablators [11-12], since they provide a relatively efficient heat protection system [13] through a variety of heat-absorbing mechanisms. First, when the material free surface is exposed to the combustion chamber hot gases, a heat-absorbing mechanism is established leading to material temperature rise [14]. As the temperature increases, the virgin material starts to degrade [15]. Part of it sublimates generating pyrolysis gases. The other portion degrades into a porous carbonaceous layer, namely char. The char itself has also an insulating effect with respect to combustion chamber high temperatures since, due to its thermal properties, it restrains the remaining part of the material from the incoming thermal loads. Such shielding effect is limited by the erosion mechanism induced by combustion gases shear stresses which cause char layer thickness reduction, therefore limiting its insulation capability. At the same time, pyrolysis gases flowing through the char to the combustion chamber environment, cool the char free surface since they are characterized by a lower temperature than the one linked to the material layer exposed to the chamber. Because of the variety of the previously mentioned phenomena, the modelling of thermal protection material behavior is challenging. The first two main models able to simulate the physics behind material ablation are CMA (Charring Material thermal response and Ablation program) [16-17] and FIAT (Fully Implicit Ablation and Thermal analysis program) [18-19]. They both rely on the 1D transient transport of thermal energy in an isotropic material, whose decomposition from virgin to char is physically identified by an Arrhenius-type relation linked to material density. Equations are numerically solved by means of the finite-difference approach. However, in CMA the numerical time discretization is explicit meaning a strong sensitivity with respect to the user time step choice. Such disadvantage is overcome in FIAT software by involving a fully implicit treatment of the equations set. More recent approaches are identified by 3D methodologies due to the need of modelling material depletion in re-entry vehicles shield. An example is represented by PATO (Porous material Analysis Toolbox) [20-22]. Its core consists of multi physics-based models which can deal with the tight coupling between hypersonic aerodynamic heating and structural heat transfer. A finite volume technique is established in the direction of solving the strong impact of hypersonic aerodynamic maintaining a low computational effort. On the contrary, finite element method approach is used among commercial programs [23-24], where material decomposition/char erosion mechanism are involved.

The present study is meant to reproduce SRM residual thrust after complete grain depletion, focusing on the impact of nozzle radiative power toward case-insulating charring ablators in a high temperature environment [25]. To do this, the first step is the development of suitable models to predict the thermal protection behavior and its impact on the tail-off thrust. A 1D ablation model has been selected in this work: the main reason relies on the axis-symmetry of SRMs case which is often cylindrical. Therefore, because of case-symmetry property, 2D or 3D effects can be considered negligible in a first-order approximation. Thus, a multi-dimensional approach does not introduce any relevant contribution to the 1D analysis. On the

contrary, 2D or 3D models are employed to achieve material ablation and depletion of more complex geometries, like re-entry vehicle shields. Furthermore, finite difference method has been exploited since it guarantees the best option in terms of computational effort for simple geometries and 1D equations. Conversely, it is practically not applicable to complex geometries linked to 2D/3D models, since the large number of mesh nodes needed to approximate the geometry local curvature implies a substantial rise of computational time.

As a second step, thermal parameters identifying the thermal protection material chosen are varied in a specific tolerance range with the aim of quantifying their influence on the residual thrust prediction. This is fundamental to evaluate how eventual measurement errors linked to thermal protection material parameters could impact on the theoretical prediction of SRM performance. In the direction of reaching the above-mentioned goals two models are employed.

1. 1D thermal protection model has been solved to identify how the ablation surface temperature is respectively linked to thermal protection material input power and pyrolysis gases mass flow rate per unit surface. These two power dependent parameters identify in a unique way the material response in terms of material reaction to the heat exchanged with SRM combustion chamber. Two set of maps respectively linked to input power and pyrolysis gases mass flow rate per unit surface are generated at different levels of power absorbed by the material itself. More specifically map inputs are represented by combustion chamber gas temperature  $T_{gas}$ , heat transfer convective coefficient  $h_c$ , and nozzle radiative power  $\dot{Q}_{noz}$ .
2. The obtained maps are integrated in ROBOOST (ROcket BOOst Simulation Tool) [2, 26], an in-house internal ballistics software which merges a 3D burning surface regression approach and a 1D unsteady fluid dynamics model linked to the combustion chamber flow.

The main outcome is the tail-off residual thrust prediction of the second solid rocket stage of Vega launcher, namely ZEFIRO 23 (Z23).

## 2. Mathematical-physical model

In this work, charring ablator material is regarded as a *continuous medium* implying that the considered phenomena are not affected by the molecular structure of the material itself and its equilibrium is governed by balance laws and constitutive relations [16]. Moreover, it is assumed that virgin material can lead to the formation of both char and pyrolysis gases only. Material melting and subsurface chemical reactions other than pyrolysis are not considered since they can be assumed negligible in a first order approximation. The above-mentioned model relies on the 1D energy transport balance through the material thickness. The terms linked to pyrolysis gas kinetic are neglected. Because of that, the momentum equation is also ignored. Moreover, it is assumed that the pyrolysis gas is in thermal equilibrium with the char layer and not chemically reacting with the char itself in any way.

Model partial differential equations are written in a moving reference frame (Figure 2): the origin of such reference frame is tied to the thermal protection free surface which recedes due to the material depletion. In particular,  $s$  is the position of the char surface, while  $L$  is the initial thermal protection thickness. The virgin material pyrolysis reaction has been described by one step reaction. Its kinetics is driven by the Arrhenius relation applied to the material density (Eq. (1)).

$$\frac{\partial \rho}{\partial t} = \dot{s} \frac{\partial \rho}{\partial x} - B \rho_v e^{-\frac{E_a}{RT}} \left( \frac{\rho - \rho_c}{\rho_v} \right)^\psi \quad (1)$$

It is important to highlight that Eq. (1) is meant to be a mass conservation relation applied to virgin material only since it characterizes how the virgin material degrades into char.

Equation (2) represents the mass conservation balance among pyrolysis gases (identified by the term  $M_g$ ), virgin and char material. More in detail, the term  $\frac{\partial M_g}{\partial x}$  expresses the variation of pyrolysis gas mass flow rate per unit surface along the spatial direction  $x$  (Figure 2). On the contrary, the term  $\frac{\partial \rho}{\partial t} - \dot{s} \frac{\partial \rho}{\partial x}$  represents the variation of solid material density during the degradation from virgin to char. Thus, Eq. (2) implies that there exists a portion of material that sublimates into a gaseous product, i.e., pyrolysis gases which occur at each point along spatial direction  $x$  where the material reaches a sufficiently high temperature.

$$\frac{\partial \rho}{\partial t} = \dot{s} \frac{\partial \rho}{\partial x} + \frac{\partial M_g}{\partial x} \quad (2)$$

Equation (3) identifies the energy conservation balance (expressed in the moving reference frame) which involves the thermal energy stored in the solid part ( $\frac{\partial(\rho H)}{\partial t} - \dot{s} \frac{\partial(\rho H)}{\partial x}$ ), the energy flux due to the pyrolysis gas motion ( $\frac{\partial(M_g H_g)}{\partial x}$ ) and the energy flux due to conduction within the material ( $\frac{\partial}{\partial x} \left( k \frac{\partial T}{\partial x} \right)$ ).

$$\frac{\partial(\rho H)}{\partial t} = \frac{\partial}{\partial x} \left( k \frac{\partial T}{\partial x} \right) + \dot{s} \frac{\partial(\rho H)}{\partial x} + \frac{\partial(M_g H_g)}{\partial x} \quad (3)$$

By rearranging the terms of Eq. (3) [16,17], it is possible to obtain Eq. (4). Such expression (Eq. (4)) is more convenient to be solved since all the terms corresponding to thermal protection material parameters (like  $\rho_v$ ,  $\rho_c$ ,  $k_v$ ,  $k_c$ ,  $c_{pg}$ ,  $H_g$ ) appear explicitly. Moreover, Eq. (4) emphasizes more directly the temperature dependance of material thermal properties (specific heat at constant pressure, thermal conductivity, formation enthalpy and density): this clarifies why thermal conductivity temperature derivatives ( $\frac{dk_v}{dT}$ ,  $\frac{dk_c}{dT}$ ) are required.

$$\begin{aligned} \frac{\partial T}{\partial t} = \frac{1}{\alpha \rho - \beta} \left\{ (H_g - \bar{H}) \frac{\partial M_g}{\partial x} + \left[ \dot{s}(\alpha \rho - \beta) + M_g c_{pg} + \frac{\xi}{\rho^2} \frac{\partial \rho}{\partial x} + \left( \frac{\rho_v}{\rho_v - \rho_c} \left( 1 - \frac{\rho_c}{\rho} \right) \left( \frac{dk_v}{dT} - \right. \right. \right. \right. \\ \left. \left. \left. \frac{dk_c}{dT} \right) + \frac{dk_c}{dT} \right) \frac{\partial T}{\partial x} \right] \frac{\partial T}{\partial x} + \left( \eta - \frac{\xi}{\rho} \right) \frac{\partial^2 T}{\partial x^2} \right\} \end{aligned} \quad (4)$$

where:

$$\alpha = \frac{C_{pv} \rho_v - C_{pc} \rho_c}{\rho_v - \rho_c} \quad (5)$$

$$\beta = (C_{pv} - C_{pc}) \frac{\rho_v \rho_c}{\rho_v - \rho_c} \quad (6)$$

$$\xi = (k_v - k_c) \frac{\rho_v \rho_c}{\rho_v - \rho_c} \quad (7)$$

$$\eta = \frac{\rho_v k_v - \rho_c k_c}{\rho_v - \rho_c} \quad (8)$$

$$\bar{H} = \frac{\rho_v H_v - \rho_c H_c}{\rho_v - \rho_c} \quad (9)$$

Pyrolysis gases, char and virgin material specific enthalpies are described respectively by the Eq.s (10), (11) and (12):

$$H_g = H_g^0 + \int_{T_0}^T C_{p_g}(T') dT' \quad (10)$$

$$H_v = H_v^0 + \int_{T_0}^T C_{p_v}(T') dT' \quad (11)$$

$$H_c = H_c^0 + \int_{T_0}^T C_{p_c}(T') dT' \quad (12)$$

Since recession rate  $\dot{s}$  is linked to the char layer, its definition is consistent with Eq. (13). The regression rate has been estimated through the Eq. (14) obtained with the following assumption [17]: thermal protection is considered in a steady state condition implying that the char recession has the same speed of the pyrolysis region. Therefore, according to mass conservation,  $(M_c + M_g(t, x = 0))$  is equal to  $\rho_v \dot{s}$  meaning that virgin material ( $\rho_v \dot{s}$ ) degrades into char ( $M_c$ ) and pyrolysis gas ( $M_g(t, x = 0)$ ).

$$M_c = \dot{s} \rho_c \quad (13)$$

$$M_c + M_g(t, x = 0) = \rho_v \dot{s} \quad (14)$$

Hence, substituting the Eq (13) into Eq. (14), it is possible to obtain Eq. (15)

$$\dot{s} = \frac{M_g(t, x = 0)}{\rho_v - \rho_c} \quad (15)$$

Equation (16) regards char free surface position.

$$s = \int_0^t \dot{s}(t') dt' \quad (16)$$

Equations (1), (2), (4) to (12), (15), (16) identifies the mathematical-physical model of the thermal protection material ablation. The solution vector consists of the following unknowns depending on time  $t$  and spatial direction  $x$ : the material density  $\rho(t, x)$ , the material temperature  $T(t, x)$ , and the mass flow rate per unit surface of pyrolysis gases  $M_g(t, x)$ . In the direction of establishing a solvable Boundary Value Problem (BVP), some initial and boundary conditions are required to determine the previously explained solution functions. Referring to initial conditions, the material has been assumed at ambient temperature ( $T_I$ , in Eq. (17)). Hence, no pyrolysis reaction occurs (mass flow rate per unit surface of pyrolysis gases is equal to 0, Eq. (18)) and the initial density along spatial coordinate is equal to virgin material density ( $\rho_v$ , in Eq. (19)).



$$T(t = 0, x) = T_I \quad (17)$$

$$M_g(t = 0, x) = 0 \quad (18)$$

$$\rho(t = 0, x) = \rho_v \quad (19)$$

Besides, boundary conditions are (Eq. (20) and Eq. (21)):

$$M_g(t, x = L - s) = 0 \quad (20)$$

$$\dot{Q}_{conv} + \dot{Q}_{rad_{in}} - \dot{Q}_{rad_{out}} - \dot{Q}_{out} + \dot{Q}_{in} - \dot{Q}_{cond} = 0 \quad (21)$$

Equation (20) is established at the end of the virgin material ( $x = L - s$ ) next to the SRM wall (Figure 2). At this point, no pyrolysis gas flow crosses the wall, thus the pyrolysis gases mass flow rate per unit surface ( $M_g$ ) is zero. Equation (21) shows the power balance (Figure 3) at the char free surface ( $x = 0$ ). It consists of the following terms:  $\dot{Q}_{conv}$ ,  $\dot{Q}_{rad_{in}}$ ,  $\dot{Q}_{rad_{out}}$ ,  $\dot{Q}_{out}$ ,  $\dot{Q}_{in}$ ,  $\dot{Q}_{cond}$ .

$\dot{Q}_{conv}$  is linked to the convective power per unit surface (Eq. (22)) exchanged between combustion chamber hot gases at temperature  $T_{gas}$  and char surface at temperature  $T(t, x = 0)$ . The heat transfer convective coefficient  $h_c$  has been corrected with the term  $\frac{\varphi}{e^{\varphi} - 1}$  (where  $\varphi$  is defined by Eq. (23)) in the direction of considering the blowing effect [16] due to pyrolysis gases injection into the combustion gases boundary layer. In Eq. (23)  $\lambda$  is a parameter depending on the combustion gases flow regime. A value of  $\lambda = 0.4$  appears to be satisfactory to correlate constant-properties turbulent flow data [16].

$$\dot{Q}_{conv} = h_c \frac{\varphi}{e^{\varphi} - 1} (T_{gas} - T(t, x = 0)) \quad (22)$$

$$\varphi = \frac{2\lambda (M_c + M_g(t, x = 0)) C_{p_{gas}}}{h_c} \quad (23)$$

$\dot{Q}_{rad_{in}}$  (Eq. (24)) and  $\dot{Q}_{rad_{out}}$  (Eq. (25)) represent respectively the radiative power per unit surface entering the material and the radiative power emitted by the char free surface.

$$\dot{Q}_{rad_{in}} = \alpha_s \sigma \varepsilon_{gas} T_{gas}^4 + \tau V_F \dot{Q}_{noz} \quad (24)$$

$$\dot{Q}_{rad_{out}} = \sigma \varepsilon_{TP} T^4(t, x = 0) \quad (25)$$

The entering radiative power is the sum of two contributions. The first one ( $\alpha_s \sigma \varepsilon_{gas} T_{gas}^4$ ) regards the power emitted by the combustion gases. It is important to highlight that the coefficient  $\alpha_s$  determines the ablative material absorptivity exposed to a two-phase gas mixture where one phase is gaseous, and the other one relies on monodispersed alumina particles [27]. The second one ( $\tau V_F \dot{Q}_{noz}$ ) is linked to the amount of power radiated by the nozzle region and absorbed by thermal protection material. It depends on the power radiated by the nozzle  $\dot{Q}_{noz}$ , the view factor of the thermal protection surface with respect to the nozzle  $V_F$ , and the gas shielding effect  $\tau$  directly proportional to the optical length.  $\dot{Q}_{noz}$  is estimated by the software ROBOOST [26], through the energy balance among the inner region of the nozzle material, its

surfaced exposed to hot gases and the convective/radiative heat coming from grain combustion. At the beginning of grain combustion, the nozzle starts to absorb heat from the combustion chamber and at the same time to radiate power to the portion of SRM thermal protection already exposed to combustion chamber hot flow. However, regarding combustion quasi-steady state phase, nozzle radiative flux does not highly affect the insulating material due to the shielding effect of grain combustion gases. A factor  $\tau$  has been multiplied to  $\dot{Q}_{noz}$  in order to integrate gas shielding effect in the overall model.  $\tau$  mainly depends on the combustion chamber pressure through a linear relation [28]. According to gases optical length, it is supposed to be near 0 when it is expected to have a small optical length (during quasi-steady state phase of propellant combustion since the pressure reaches high values). On the contrary, for low pressure values, the optical length increases implying that  $\tau$  increases up to 1. Such scenario is typical for the tail-off phase when, at the end of grain combustion, the pressure rapidly decreases. However, even at the tail-off phase when the shielding factor is close to 1, not all the power emitted by the nozzle reaches the thermal protection material. Only a portion of radiation leaving the nozzle surface strikes the exposed material surface. Such amount of radiation heat depends on how the nozzle is positioned with respect to the material region considered. In the direction of evaluating such effect, a local view factor distribution ( $V_F$  in Figure 4) along motor axis  $z$  (Figure 1c) has been determined through a commercial software [29]. To compute the local view factor  $V_F$ , Z23 thermal protection case has been split into 34 annular sections orthogonal to the motor axis. Then,  $V_F$  belonging to each section has been obtained [29].

The algebraic sum of  $\dot{Q}_{in} - \dot{Q}_{out}$  (Eq. (26) and Eq. (27)) corresponds to the net chemical energy flux entering and exiting the char surface.  $\dot{Q}_{in}$  (Eq. (26)) represents the energy flux brought to the char surface through the transport of pyrolysis gases ( $M_g(t, x = 0)H_g(T = T(t, x = 0))$ ) produced in the pyrolysis region of the material (Figure 2) and through the char formation process ( $M_c H_c(T = T(t, x = 0))$ ). On the other hand,  $\dot{Q}_{out}$  relies on the blowing effect of pyrolysis gases leaving the char surface. Such gas flow causes the gross motion of combustion gases within the boundary layer adjacent to the char surface. The combustion gases specific enthalpy, i.e.,  $H_{gas}^0 + \int_{T_0}^{T(t, x=0)} c_{p_{gas}}(T')dT'$ , has been included in Eq. (27) in order to appropriately evaluate the exiting power per unit surface  $\dot{Q}_{out}$ .

$$\dot{Q}_{in} = M_c H_c(T = T(t, x = 0)) + M_g(t, x = 0)H_g(T = T(t, x = 0)) \quad (26)$$

$$\dot{Q}_{out} = -(M_c + M_g(t, x = 0)) \left( H_{gas}^0 + \int_{T_0}^{T(t, x=0)} c_{p_{gas}}(T')dT' \right) \quad (27)$$

Finally,  $\dot{Q}_{cond}$  (Eq. (28)) is linked to the power per unit surface entering the material at the free surface ( $x = 0$ ). The thermal conductivity associated to the free surface, i.e., ( $k(t, x = 0)$ ) is defined as the weighted average with respect to the virgin and char material thermal conductivity (respectively  $k_v$  and  $k_c$ ). Equation (29) is fundamental to properly represent the transition of the free surface from virgin to char. In fact, before ablation, the free surface consists of virgin material only, then  $\rho = \rho_v$ . The mass fraction of virgin material  $X$  (Eq. (30)) turns out to be 1 leading to  $k = k_v$ . On the contrary, when the char is completely formed,  $\rho = \rho_c$  resulting in  $k = k_c$ . During char formation at the free surface,  $k$  assumes an intermediate value, guaranteeing a smooth transition between the two extremes represented by  $k_v$  and  $k_c$ . Pyrolysis gas, virgin material and char material properties are referred to thermal protection material X3600, whose experimental values were established in [31].

$$\dot{Q}_{cond} = -k(t, x = 0) \frac{\partial T}{\partial x} \Big|_{t, x=0} \quad (28)$$

$$k(t, x) = X(t, x)k_v + (1 - X(t, x))k_c \quad (29)$$

$$X(t, x) = \frac{\rho_v}{\rho_v - \rho_c} \left( 1 - \frac{\rho_c}{\rho} \right) \quad (30)$$

### 3. Algorithm overview

The procedure used in the present work consists of three steps. First, the thermal protection ablation model (Eq.s (1), (2), (4)) is solved according to different values of  $h_c$ ,  $T_{gas}$  and  $\dot{Q}_{noz}$  and the results are collected into maps. Second, such maps are included in an in-house internal ballistics simulation software, namely ROBOOST [26], in order to estimate Z23 residual thrust and to compare such thrust with the experimental data. The main goal of the above-mentioned step is the validation of the strategy chosen to evaluate the residual thrust. Third, a sensitivity analysis is performed by varying some properties of thermal protection material such as virgin and char material constant pressure specific heat, i.e.,  $c_{p_v}$  and  $c_{p_c}$ , and virgin and char material thermal conductivity, i.e.,  $k_v$  and  $k_c$ .

Regarding the first step of the above-mentioned procedure, the finite difference technique has been applied to the BVP concerning thermal protection ablation. A 4<sup>th</sup> order numerical scheme along spatial coordinate  $x$  has been selected as a trade-off between the accuracy of the solution and the computational effort needed to obtain the solution vector  $(\rho, T, M_g)$ . More specifically, Eq. (1) and Eq. (2) relies on a 4<sup>th</sup> order forward difference since the information propagates from the left ( $x = 0$ ) to the right side ( $x = L - s$ ) of the domain. On the other hand, a 4<sup>th</sup> order centered scheme allows the solution of Eq. (4) where the heat diffusion mechanism prevails in all directions. Because of the high degree of stiffness of this BVP, a 2<sup>nd</sup> order backward difference formula has been assumed to approximate the partial derivative in time. The time step and the spatial step of each simulation performed are respectively  $1 \cdot 10^{-4} s$  and  $2 \cdot 10^{-2} mm$ , and they are maintained constant according to a uniform grid both in space and time. It is fundamental to notice that the choice of time step is not relevant for the map usage in ROBOOST, but it has been appropriately determined to obtain enough accurate results regarding the numerical solution of thermal protection BVP. The ablation physical model is set up with ambient temperature and pressure as initial conditions. Since such values greatly differ from actual working condition of Z23, the steady-state condition for each simulation has been retained, at approximately 15s. Moreover, three external parameters, i.e.,  $h_c$ ,  $T_{gas}$ ,  $\dot{Q}_{noz}$ , enter the BVP. Different values of such parameters are established with the aim of capturing the working condition of Z23 combustion chamber at tail-off.  $h_c$  belongs to the interval  $[0, 1500] W/m^2K$ , where  $1500 W/m^2K$  is a typical value of the quasi-steady state phase of combustion; instead  $0 W/m^2K$  is the limit value when the grain combustion is over.  $T_{gas}$  varies between  $T_l = 293 K$  and  $3500 K$ . The latter is the temperature reached in the combustion chamber during grain burning. Finally,  $\dot{Q}_{noz}$  belongs to the interval  $[0, 3.7] MW$ , where  $3.7 MW/m^2$  is the maximum power per unit surface emitted by the portion of nozzle within the combustion chamber (Figure 1d). For each combination of  $h_c$ ,  $T_{gas}$ ,  $\dot{Q}_{noz}$ , the BVP solution vector  $(\rho, T, M_g)$  has been computed. Subsequently, the results are combined into maps. Each map input is represented by the triplet  $h_c, T_{gas}, \dot{Q}_{noz}$ ; instead, the outputs are the following ones: the free surface temperature  $T(t, x = 0)$ , the mass flow rate per unit surface of pyrolysis

gases  $M_g(t, x = 0)$  exiting the material, and the power per unit surface ( $\dot{Q}_{abs}$ ) absorbed by thermal protection material from the combustion chamber. Furthermore, it is fundamental to highlight that the evaluation of  $h_c$ ,  $T_{gas}$ ,  $\dot{Q}_{noz}$  has been performed by means of ROBOOST software [26].  $h_c$  prediction relies on the Dittus-Boelter formula [30], shown with Eq.s (31) and (32).  $K_{Nu}$  has been appropriately set equal to 0.023 according to [30].

$$h_c = k_{gas} \frac{Nu}{Pr} \quad (31)$$

$$Nu = K_{Nu} Re^{0.8} Pr^{0.4} \quad (32)$$

$T_{gas}$  is estimated in accordance with propellant thermochemical properties obtained through NASA CEA (Chemical Equilibrium and Applications) program. Such properties are included in the energy balance equation [26] of the combustion chamber in order to evaluate the gas temperature distribution along the motor axis  $z$  (Figure 1c). This allows a local estimation of  $T_{gas}$ , which is essential to compute the local contribution of pyrolysis gases injected in the combustion chamber. Finally, the power per unit surface radiated by the nozzle ( $\dot{Q}_{noz}$ ) is determined by considering the heat balance between the nozzle and the combustion chamber, as outlined in the previous paragraph. To verify that steady-state values of the maps can describe the strong time variations occurring at tail-off of the quantities  $h_c$ ,  $T_{gas}$ ,  $\dot{Q}_{noz}$  some simulations have been performed. Figure 5 shows how char recession rate varies with time when a step change of nozzle power per unit surface is applied to the thermal protection at steady-state initial conditions. The blue line is computed with an amount of nozzle radiative power ( $\dot{Q}_{noz_1}$ ) corresponding to the maximum power absorbed by thermal protection material. Since maps input parameters ( $h_c$ ,  $T_{gas}$ ,  $\dot{Q}_{noz}$ ) are strongly time-dependent due to the unsteadiness of tail-off phase, the thermal protection material response has been evaluated between these two levels of nozzle radiative power (0 and  $\dot{Q}_{noz_1}$  in Figure 5). A step variation (between 0 and  $\dot{Q}_{noz_1}$ ) of nozzle power per unit surface has been applied to the red curve (Figure 5) to reach the power level of the blue curve. The time scale needed for the thermal protection material to adapt to the new power condition is about 0.1 s., at least two order of magnitude lower than tail-off time scale in the order of tens of seconds. Furthermore, the char recession rate overshoot at 5 s (green curve) is about 0.8% larger than the corresponding value on the red curve, meaning that such overshoot is negligible. The same consideration can be stated for  $h_c$ ,  $T_{gas}$  since these quantities are part of the thermal protection absorbed power (Eq. (21)), in a similar way to  $\dot{Q}_{noz}$ .

The second step is focused on model validation comparing simulation result with experimental data in terms of Z23 residual thrust. To reach that goal, an in-house simulation software, namely ROBOOST [26], is used to estimate Z23 tail-off. More specifically, such software consists of three modules, i.e., *grain regression module*, *ballistics module* and *thermal protection maps module*. The *grain regression module* determines the burning surface shape during grain combustion. The burning surface is discretized as a 3D triangular mesh where each mesh node is managed independently with respect to the others. In general, an unstructured mesh is employed, where the size and number of triangles depends on the complexity of the SRM shape. In addition to that, mesh vertices are properly displaced in space according to the local value of the burned web. The displacement direction is orthogonal to the local vertex. To determine such direction, the software relies on the linear combination of the normals belonging to the triangles adjacent to the vertex considered [26]. On the contrary, vertices lying on the case are forced to move along the case profile only. The above-mentioned mesh strategy

allows both the evaluation of the local thermal protection material surface ( $A_{TP}$ ) exposed to combustion gases and the local mass flow rate of grain burned ( $\dot{m}_p$ ), as shown in Figure 6. The *ballistics module* is based on a 1D unsteady fluid dynamic model which allows the estimation of combustion chamber flow quantities (the main ones are flow speed, pressure, temperature) and SRM performance parameters (characteristic velocity, thrust coefficient, thrust). This module both interacts with the *grain regression module* providing it with the burning rate ( $r_b$ ) essential to estimate the amount of grain mass flow rate injected within the combustion chamber, and the *thermal protection maps module* guaranteeing the instantaneous values of maps input parameters ( $h_c$ ,  $T_{gas}$ ,  $\dot{Q}_{noz}$ ). Finally, *thermal protection maps module* contains the insulating material maps generated at the first step of the overall procedure. More specifically, it supplies the *ballistics module* with pyrolysis gas mass flow rate ( $\dot{m}_g$ ) and the insulating material absorbed power from the combustion chamber ( $\dot{Q}_{abs}$ ). These two values are included in the mass balance and energy balance equations of ROBOOST internal ballistics model [26] with the aim of computing Z23 residual thrust. It is of fundamental importance to highlight ROBOOST capability to predict the 3D exposure and consumption of thermal protection insulating material. In fact, due to the 3D triangular mesh regression linked to the burning surface, the software can compute the thermal protection material local consumption at the case. For each insulating material layer local point, when the local grain amount is consumed, material ablation begins. Hence, for such SRM zones identified by an earlier grain burn-out (for instance the fynocil part near the nozzle in Figure 1a and Figure 1c), the material starts to experience a prior ablation with respect to the cylindric portion of the combustion chamber. The main consequence is that the thermal protection corresponding to the cylindrical part of the combustion chamber is the most responsible of residual thrust production since the pyrolysis gas contribution of the material located at the fynocil part is lower compared to the previous part in consideration of the fact that such portion consists of mostly char. Moreover, as already pointed out in the previous paragraph, the local heat absorbed by thermal protection is adequately evaluated by means of the view factor: because Z23 geometry is axisymmetric, it is sufficient to consider a view factor distribution varying along motor axis only. A deeper ROBOOST explanation can be found in [26]. However, it is important to emphasize that ROBOOST software has already been validated [26] on another SRM, namely ZEFIRO 9. Regarding the third step, the insulating material properties chosen for the sensitivity analysis are the following ones:  $c_{pv}$ ,  $c_{pc}$ ,  $k_v$ ,  $k_c$ . Heat transfer convective coefficient has been also selected as parameter for such sensitivity analysis since it is considered as a challenging quantity to be estimated both theoretically and with experiments. Each parameter is varied of an amount corresponding to  $\pm 20\%$ . Only  $h_c$  is varied of  $\pm 50\%$  by increasing and decreasing  $K_{Nu}$  of such percentual variation. At this point, the corresponding thermal protection maps are determined according to step 1. Then, ROBOOST simulation is performed (step 2) in order to obtain the residual thrust curve corresponding to each variation. By repeating step 1 and step 2 for all the selected material quantities, it is possible to determine a fluctuation band around the actual Z23 residual thrust trend showing the impact of possible measurement uncertainties regarding material thermal properties on performance prediction.

## 4. Results

The previously explained procedure has been applied to Z23. More specifically, the main dimensions of this solid rocket motor are a height of 7.5 m and a diameter of nearly about 2m. Moreover, it is filled with 24 tons of HTPB-based composite propellant in a fynocil-cylinder configuration. The cylinder grain geometry is placed in the fore and central parts of the rocket at the igniter side (Figure 1); on the contrary the fynocil shape is positioned in the rear part near the nozzle inlet (Figure 1).

The charring ablator chosen is X3600 [31], which consists of a carbon-phenolic composition. Its thermochemical properties are shown in Table 1 together with other useful initialization data. Considering such material, the thermal protection BVP has been solved for different values of  $h_c$ ,  $T_{gas}$ ,  $\dot{Q}_{noz}$  according to step 1 of the procedure previously outlined. The results are collected in a series of maps, each one corresponding to a specific value of  $\dot{Q}_{noz}$ . Figure 7a, b and Figure 7c, d respectively show thermal protection material maps without and with nozzle radiation contribution, each one computed at 5 different levels of heat transfer convective coefficient  $h_c$ . More specifically, the map regarding radiation contribution has been computed by considering maximum Z23 view factor, i.e., 0.15 (Figure 4). Non dimensional mass flow rate per unit surface of pyrolysis gases ( $M_g(t, x = 0)$ ) and thermal protection absorbed power ( $\dot{Q}_{abs}$ ) from the combustion chamber are scaled respectively with the maximum values belonging to the map which includes nozzle radiation contribution (Figure 7c, d). Besides, it is fundamental to emphasize that the above-mentioned maps are two of a larger set of maps where each one is obtained at intermediate levels of radiative power produced by the nozzle region within the combustion chamber.

Some considerations can be raised on the above-mentioned maps. Comparing Figure 7a and Figure 7b, it can be noticed that the material ablation leading to pyrolysis gases production has an higher intensity with nozzle radiation than without it. In fact, the maximum value of  $M_g(t, x = 0)$  corresponding to Figure 7b is higher than the one linked to Figure 7a. On the contrary, the maximum absorbed power by the insulating material, i.e.,  $\dot{Q}_{abs}$ , without nozzle radiation (Figure 7d) is lower if compared with the case regarding nozzle power contribution (Figure 7b). Such effect relies on the fact that  $\dot{Q}_{abs}$  represents the net power exchanged between thermal protection material and the SRM combustion chamber only. Indeed, if no nozzle contribution is included, the ablation is sustained by combustion chamber power only, therefore the entire amount of heat absorbed comes from the combustion chamber. On the other hand, when the nozzle radiation process starts, a portion of the heat needed for ablation is produced by the nozzle itself, hence it is evident that after burn-out time instant, the combustion chamber input is absent and only radiative effect is prominent. Moreover, it must be emphasized that, at tail-off when the propellant combustion is almost over and hot gas convection does not occur anymore (i.e.,  $h_c$  is close to zero, light blue curve in Figure 7), nozzle radiation is the only effect sustaining material ablation (Figure 7c). This is confirmed by Figure 7a where for typical values of tail-off hot gas temperature (i.e.,  $T_{gas}$  lower than 2000 K), a nearly-zero amount of pyrolysis gases is produced. The above-mentioned observations highlight the fundamental role of nozzle radiative power after burn-out.

The negative power reached by the absorbed power in Figure 7d is also meaningful. In fact, as previously mentioned,  $\dot{Q}_{abs}$  represents the net power exchanged between the insulating material and the combustion chamber environment. As a matter of facts, there could be a limit case when if the nozzle radiation is strong and the gas temperature is low, thermal protection material temperature could be higher than  $T_{gas}$ , hence heat exchange occurs in the opposite direction, i.e., from the material to the combustion chamber. For instance, such extreme condition is reached at tail-off when the grain is completely depleted.

Subsequently, maps obtained at step 1 are included in ROBOOST software to determine Z23 residual thrust – time profile. Figure 8 shows such result, where thrust has been scaled with respect to the maximum thrust measured and the percentual error identifies the relative percentual error with respect to experimental data relying on Z23 flight test. The time axis starts at the time instant corresponding to a combustion chamber pressure of 1 bar. Maximum percentual error is close to 0.01% meaning that there is an acceptable match between simulation and experimental data. It is fundamental to highlight that the residual thrust prediction is essential for the proper sequence of stage separation. In fact, although the amount of residual

thrust is low if compared to the propellant-produced thrust, it acts for a not negligible time range in the order of twenty seconds (Figure 8). The above-mentioned statement implies that if stages separation times are not properly designed, the detached stage could strike the remaining part of the launcher probably causing mission failure. Hence, the amount residual thrust, and its time duration should be considered in order to achieve the right interstage wait times.

Moreover, the entire procedure is validated, and a well posed sensitivity analysis can be computed. Figure 9 shows different residual thrust profiles, each one corresponding to the variation of the following parameters:  $c_{pv}$ ,  $k_v$ ,  $k_c$  and  $h_c$ . More specifically, non-dimensional residual thrust is defined as the ratio between the residual thrust corresponding to each curve and the experimental maximum residual thrust, in a similar way to Figure 8.

Among such curves, the most noticeable effect is given by the variation of  $c_{pv}$ . Indeed, a high value of  $c_{pv}$  implies that more time is needed by the insulating material to reach ablation condition, since more heat is required to increase material temperature. For that reason, material depletion is slow-moving, and the amount of pyrolysis gases produced is low as well. As the total amount of pyrolysis gas mass flow rate injected in the combustion chamber is lower than the one linked to the nominal curve (red curve in Figure 9), the computed residual thrust (blue curve in Figure 9) assumes lower values if compared to the nominal one. On the contrary, low values of  $c_{pv}$  lead to a more intense production of pyrolysis gases since a low amount of time is required by thermal protection material to reach ablation condition. However, this effect occurs only at the beginning of thrust production when a small amount of char is present. When char layer thickness is large enough, the power reaching the ablation layer decreases, implying a deceleration of the ablation process. In such conditions, for instance occurring at tail-off phase, pyrolysis gas mass production also decreases with respect to the nominal case, thus justifying the lower amount of residual thrust with respect to the one represented by the nominal curve. However, residual thrust corresponding to a decrease of  $c_{pv}$  is higher than the one linked to a decrease of  $c_{pv}$ . This depends on the fact that the char influence on pyrolysis gas production is counteracted by the material ablation occurring faster in the former case with respect to the latter.

Regarding the effect of the virgin material thermal conductivity, it can be highlighted that an increase of  $k_v$  (yellow curve in Figure 9) has no effect on residual thrust since a saturation condition of the ablation process has been reached, meaning that even if more power is conducted through the material thickness, due to an increase of  $k_v$ , time amount to reach the ablation condition remains the same. On the contrary, a small decrease of  $k_v$  implies a small decrease of the residual thrust curve.

Concerning  $k_c$ , the increment or decrease of such quantity influences the power arriving at the pyrolysis region, leading to an increment or decrease of pyrolysis gas production. As it is expected, the above-mentioned effect causes a rise or reduction of residual thrust.

Finally, the heat transfer convective coefficient  $h_c$  does not have any appreciable effect on the residual thrust behavior, since at tail-off the combustion is over and the hot gas velocity within the combustion chamber is near zero. For that reason, the two curves corresponding to  $h_c$  variation are very close to the nominal one (Figure 9). This means that an error on the evaluation of  $h_c$  does not affect in a relevant way the prediction of SRM performance.

## 5. Conclusions

A numerical procedure has been proposed to obtain Z23 residual thrust profile and to perform a sensitivity analysis based on insulating material thermal properties variations. First a mathematical-physical model regarding pyrolysis, ablation and char mechanical erosion has been established. Then, by varying the parameters identifying material absorbed power, i.e.,

heat transfer convective coefficient, hot gas temperature and nozzle radiated power, material model results have been collected into maps. Such maps are integrated in a in-house simulation software to compute Z23 residual thrust validating in this way the entire procedure. Finally, a sensitivity analysis has been performed in the direction of investigating the impact of possible error measurements concerning material properties.

## References

- [1] Sutton, G., P., and Biblarz, O., “*Rocket Propulsion Elements*”, New York, John Wiley & Sons Inc., pp. 1-26, 2010
- [2] Ponti, F., Mini, S., and Annovazzi, A., A Simplified Approach to Predict Friedman Curl Effect in a Solid Rocket Motor, *AIAA Propulsion and Energy Forum*, Indianapolis, IN, USA, 2019. DOI: 10.2514/6.2019-3960
- [3] Boraas, S., Hyland, B., and Smart, L., Predicted Porst Burn Residual Thrust for an Orbital Transfer Motor, *21<sup>st</sup> Joint Propulsion Conference*, Monterey, CA, USA, 1985. DOI: 10.2514/6.1985-1395
- [4] Chang, I-S., Slag and Enviroment of a Spinning Rocket Motor, *Journal of Spacecraft and Rockets*, Vol. 28(5), pp. 599-605, 1991. DOI: 10.2514/3.26286
- [5] Akiba, R., and Kohno, M., Experiments with Solid Rocket Technology in the Development of M-3SII, *Acta Astronautica*, Vol. 13(6-7), pp. 349-361, 1986. DOI: 10.1016/0094-5765(86)90090-1
- [6] Madhava Panicker, P., R, Ramachandran, N., Sreekumar, K., P., and Majeed, M., K., A., Pyrolysis Caused Tail-Off Thrust in a Solid Rocket Motor: A Semi-Empirical Model, *Defense Science Journal*, Vol. 48(1), pp. 87-91, 1998
- [7] Johnston, W., A., Murdock, J., W., Koshigoe, S., and Than, P., T., Slag Accumulation in the Titan Solid Rocket Motor Upgrade, *Journal of Propulsion and Power*, Vol. 11(5), pp. 1012-1020, 1995. DOI: 10.2514/3.23931
- [8] Haloulakos, V., E., Slag Mass Accumulation in Spinning Solid Rocket Motors, *Journal of Propulsion and Power*, Vol. 7(1), pp. 14-21, 1991. DOI: 10.2514/3.23289
- [9] Meyer, R., X., In Flight Formation of Slag in Spinning Solid Propellant Rocket Motors, *Journal of Propulsion and Power*, Vol. 8(1), pp. 45-50, 1992. DOI: 10.2514/3.23440
- [10] Boraas, S., Modeling Slag Deposition in the Space Shuttle Solid Rocket Motor, *Journal of Propulsion and Power*, Vol. 21(1), pp. 47-54, 1984. DOI: 10.2514/3.8606
- [11] Li, W., Huang, H., Tian, Y., and Zhao, Z., A Nonlinear Pyrolysis Layer Model for Analyzing Thermal Behavior of Charring Ablator, *International Journal of Thermal Sciences*, Vol. 98, pp. 104-112, 2015. DOI: j.ijthermalsci.2015.07.002
- [12] Amar, A., J., Blackwell, B., F., and Edwards, J., R., One-Dimensional Ablation Using a Full Newton’s Method and Finite Control Volume Procedure, *Journal of Thermophysics and Heat Transfer*, Vol. 22(1), pp. 71-82, 2008, DOI: 10.2514/1.29610
- [13] Bahramian, A., R., Kokabi, M., Famili, M., H., N., and Beheshty, M., H., Ablation and Thermal Degradation Behaviour of a Composite Based on Resol Type Phenolic Resin: Process Modeling and Experimental, *Polymer*, Vol. 47(10), pp. 3661-3673, 2006. DOI: j.polymer.2006.03.049
- [14] Swann, R., T., Dow, M., B., and Tompkins, S., S., Analysis of the Effects of Enviromental Conditions on the Performance of Charring Ablators, *Journal of Spacecraft and Rockets*, Vol. 3(1), pp. 61-67, 1966. DOI: 10.2514/3.28386
- [15] Mohammadiun, H., and Mohammadiun, M., Numerical Modelling of Charring Material Ablation with considering Chemical-Reaction Effects, Mass Transfer and Surface Heat



- Transfer, *Arabian Journal for Science and Engineering*, Vol. 38, pp. 2533-2543, 2013. DOI: 10.1007/s13369-012-0510-0
- [16] Schoner, R., J., User's Manual Aerotherm Charring Material Thermal Response and Ablation Program, Air Force Rocket Propulsion Laboratory, AFRPL-TR-70-92, April 1970.
  - [17] Moyer, C., B., and Rindal, R., A., An Analysis of the Coupled Chemically Reacting Boundary Layer and Charring Ablator. Part 2- Finite Difference Solution for the In-Depth Response of Charring Materials Considering Surface Chemical and Energy Balances, NASA CR-1061, June 1968
  - [18] Milos, F., S., and Chen, Y., K., Ablation, Thermal Response, and Chemistry Program for Analysis of Thermal Protection Systems, *Journal of Spacecraft and Rockets*, Vol. 50(1), pp. 137-149, 2013. DOI: 10.2514/1.A32302
  - [19] Milos, F., S., and Chen, Y., K., Ablation and Thermal Response Property Model Validation for Phenolic Impregnated Carbon Ablator, *Journal of Spacecraft and Rockets*, Vol. 47(5), pp. 786-805, 2010. DOI: 10.2514/1.42949
  - [20] Lachaud, J., Van Eekelen, T., Scoggins, J., B., Magin, T., E., and Mansour, N., N., Detailed Chemical Equilibrium Model for Porous Ablative Materials, *International Journal of Heat and Mass Transfer*, Vol. 90, pp. 1034-1045, 2015. DOI: j.ijheatmasstransfer.2015.05.106
  - [21] Lachaud, J., and Mansour, N., N., Porous-Material Analysis Toolbox Based on OpenFOAM and Applications, *Journal of Thermophysics and Heat Transfer*, Vol. 28(2), pp. 191-202, 2014. DOI: 10.2514/1.T4262
  - [22] Lachaud, J., Scoggins, B., J., Meyer, M., G., and Mansour, N., N., A Generic Local Thermal Equilibrium Model for Porous Reactive Materials submitted to High Temperatures, *International Journal of Heat and Mass Transfer*, Vol. 108, pp. 1406-1417, 2017. DOI: j.ijheatmasstransfer.2016.11.067
  - [23] Huang, J., Yao, W. X., Shan, X., Y., and Chang, C., Coupled-Fluid-Structural Thermal Numerical Methods for Thermal Protection System, *AIAA Journal*, Vol. 57(8), pp. 3630-3638, 2019. DOI: 10.2514/1.J057616
  - [24] Wang, Y., Risch, T., K., and Pasillio, C., L., Modeling of Pyrolyzing Ablation Problem with ABAQUS: A One-Dimensional Test Case, *Journal of Thermophysics and Heat Transfer*, Vol. 32(2), pp. 542-545, 2018. DOI: 10.2514/1.T5274
  - [25] Mathieu, R., D., Mechanical Spallation of Charring Ablators in Hyperthermal Environments, *AIAA Journal*, Vol. 2(9), pp. 1621-1627, 1964. DOI: 10.2514/3.2629
  - [26] Ponti, F., Mini, S., and Annovazzi, A., Numerical Evaluation of the Effects of Inclusions on Solid Rocket Motor Performance, *AIAA Journal*, Vol. 58(9), pp. 4028-4036, 2020. DOI: 10.2514/1.J058735
  - [27] Dombrovsky, L. A., "Radiation Heat Transfer in Disperse Systems," New York, Begell House Inc. Publ., pp. 145-239, 1995.
  - [28] Bodhaine, B., A., Wood, N., B., Dutton, E., G., and Slusser, J., R., On Rayleigh Optical Depth Calculations, *Journal of Atmospheric and Oceanic Technology*, Vol. 16(11), pp. 1854-1861, 1999. DOI:10.1175/1520-0426(1999)016<1854:ORODC>2.0.CO;2
  - [29] ANSYS, Inc. (2016) ANSYS Fluent User's Guide, Release 17.2
  - [30] Peretz, A., Kuo, K., Caveny, L., and Summerfield, M., The Starting Transient of Solid-Propellant Rocket Motors with High Internal Gas Velocities, *8<sup>th</sup> Joint Propulsion Specialist Conference*, New Orleans, LA, USA, 1972. DOI: 10.2514/6.1972-1119

[31] Williams, S., D., and Curry, D., M, *Thermal Protection Materials*, NASA RP-1289, December 1992.

### Images and tables

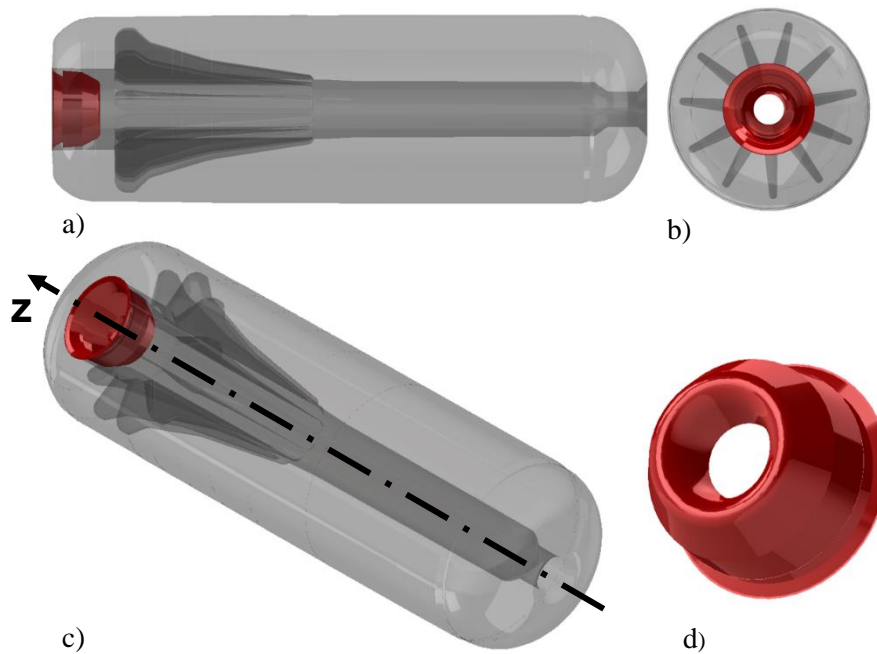


**Figure 1: ZEFIRO 23 combustion chamber layout.**

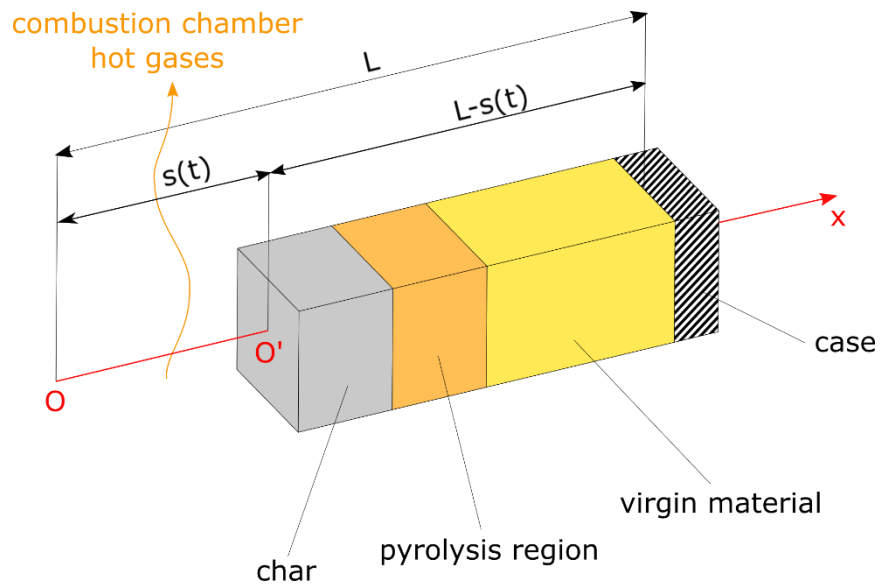


**Figure 2: Moving reference frame.**

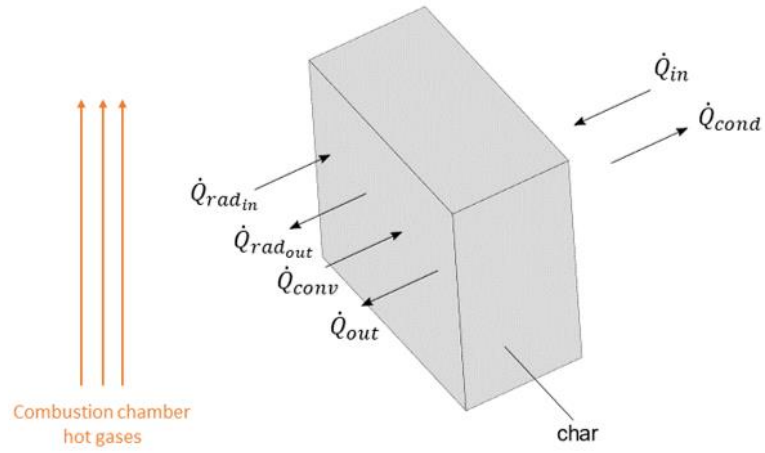


**Figure 3: Power balance at the material free surface.**

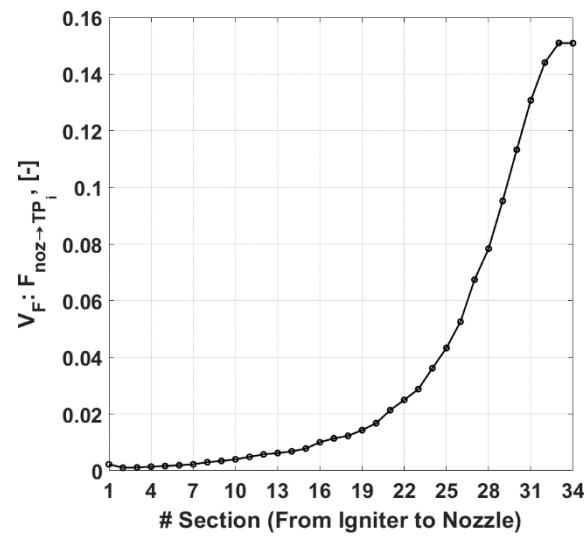


**Figure 4: View factor distribution along motor axis.**

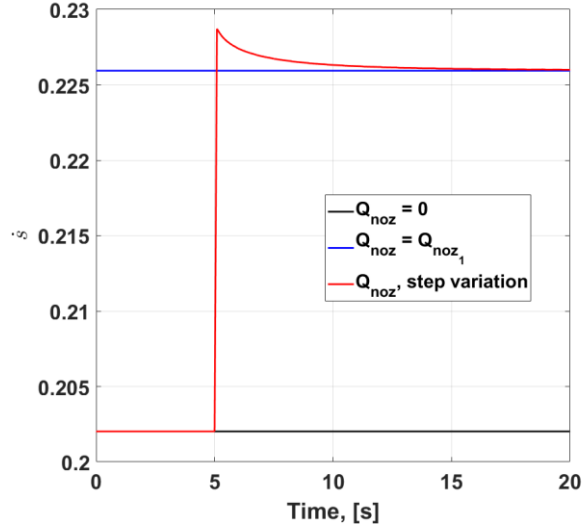


Figure 5: Thermal protection material response to nozzle power step variation.

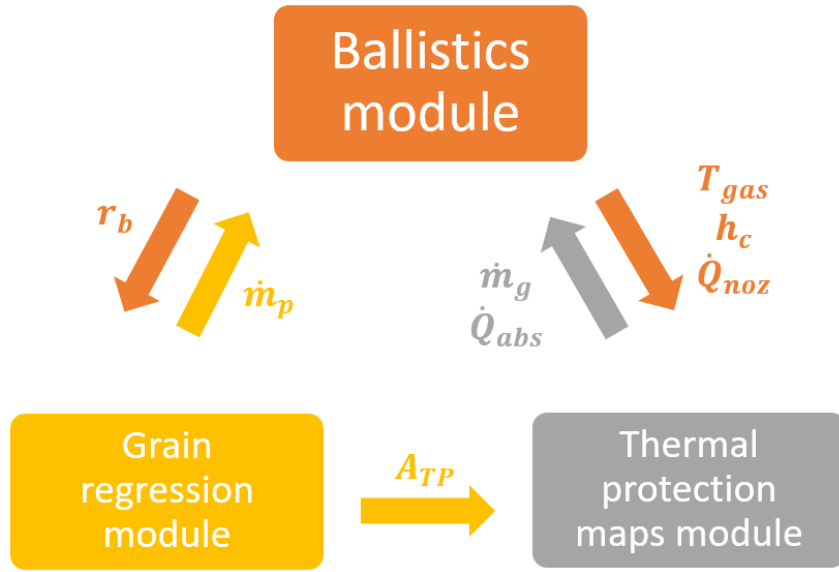


Figure 6: ROBOOST layout.

Table 1: Input parameters

Pyrolysis gas properties, [31]	Virgin material properties, [31]	Char material properties, [31]
$h_g^0$ [J/kg]: 0	$\rho_v$ [kg/m <sup>3</sup> ]: 1441.8	$\rho_c$ [kg/m <sup>3</sup> ]: 961.2
$c_{p_g}$ [J/kg · K]: 1660	$h_v^0$ [J/kg]: $-1.4 \cdot 10^6$	$h_c^0$ [J/kg]: 0
-	$c_{p_v}$ [J/kg · K]: 1038	$c_{p_c}$ [J/kg · K]: 1080
-	$k_v$ [W/m · K]: 0.53	$k_c$ [W/m · K]: 0.65

Arrhenius equation properties, [31]	
$B [1/s]: 1.82 \cdot 10^4$	
$E_a [J/mol]: 4.66 \cdot 10^4$	
$\psi [-]: 1$	
Other parameters	
$T_0 [K]: 298.15$	[31]
$T_f [K]: 293$	
$\varepsilon_{TP} [-]: 0.8$	[31]
$\alpha_s [-]: 1$	[27]
$\lambda [-]: 0.4$	[16]
$L [m]: 0.01$	
$R [J/mol \cdot K]: 8.31$	
$\sigma [W/m^2 \cdot K^4]: 5.67 \cdot 10^{-8}$	

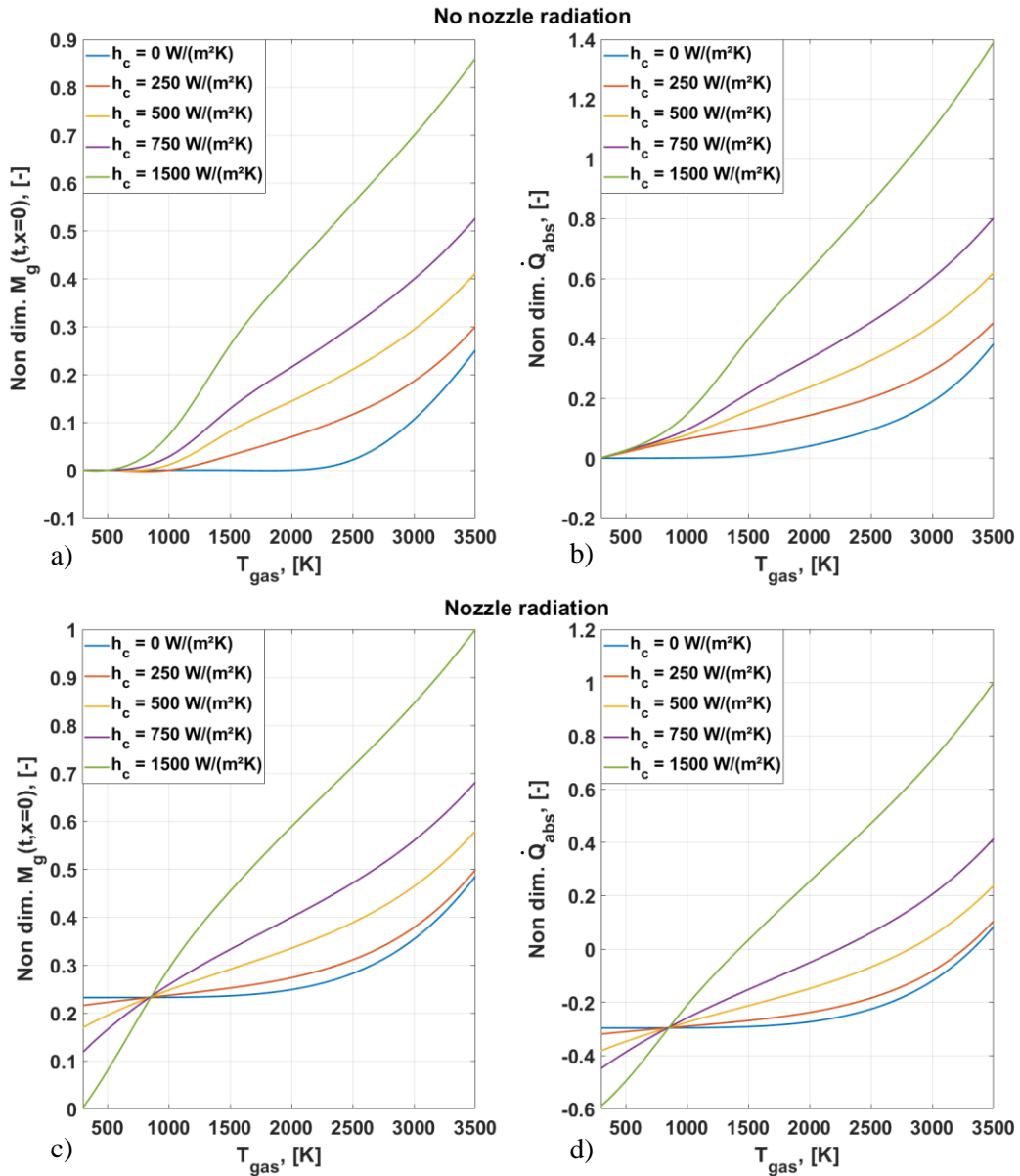
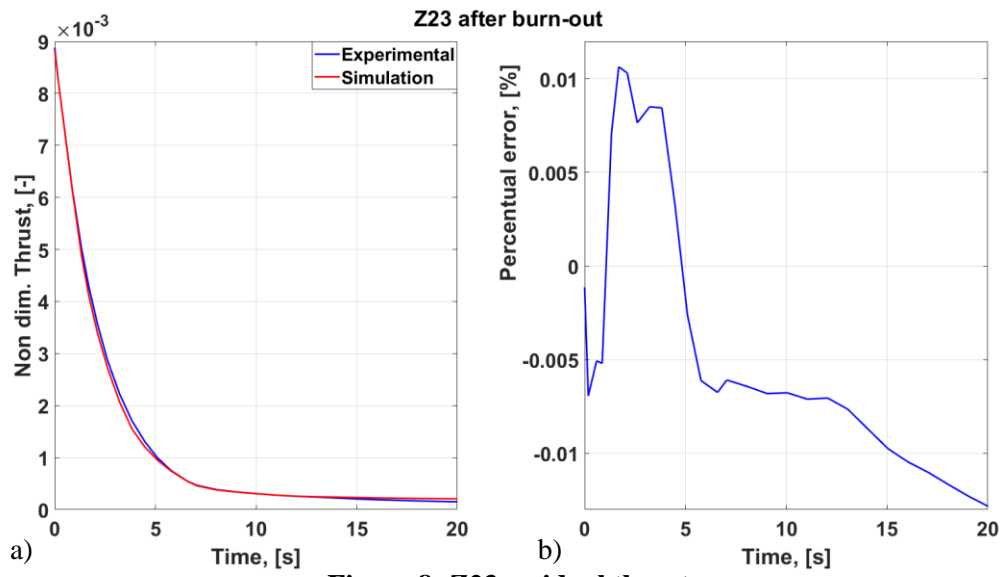
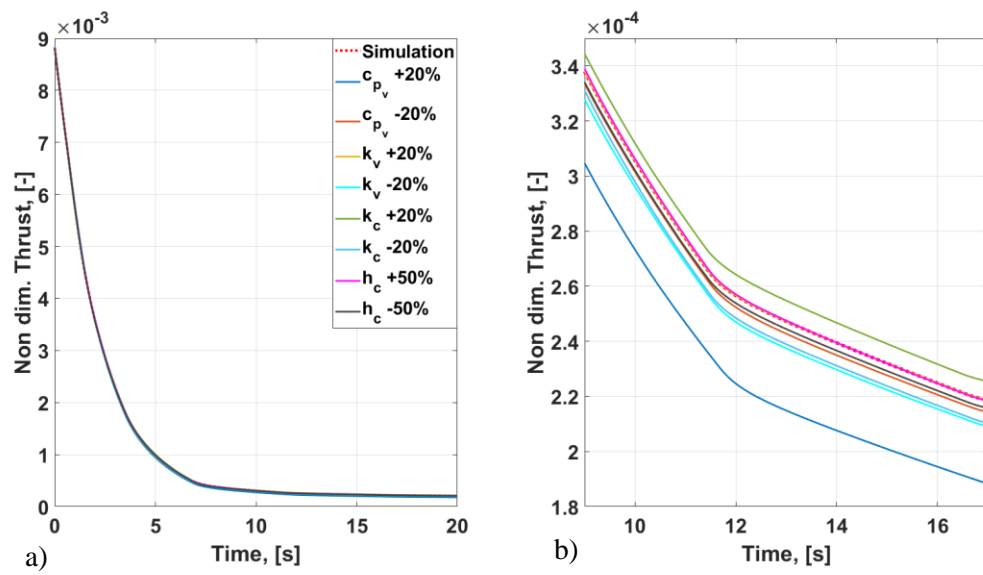


Figure 7: Thermal protection material maps.



**Figure 8: Z23 residual thrust.**



**Figure 9: Residual thrust sensitivity analysis.**